RSC Advances

ROYAL SOCIETY OF CHEMISTRY

PAPER

View Article Online
View Journal | View Issue

Check for updates

Cite this: *RSC Adv.*, 2020, **10**, 43193

Facile synthesis of multi-type carbon doped and modified nano-TiO_2 for enhanced visible-light photocatalysis†

Jianing Li,[ab] Junzhong Wang,[b] Juming Liu,*[ab] Yan Li,[b] Huiyan Ma,[ab] Jucai Yang[ac] and Qiancheng Zhang*[ab]

Received 19th October 2020
Accepted 20th November 2020

DOI: 10.1039/d0ra08894c

rsc.li/rsc-advances

Nano-TiO_2 is a type of environment-friendly and inexpensive substance that could be used for photocatalytic degradation processes. In this study, the multi-type carbon species doped and modified anatase nano-TiO_2 was innovatively synthesized and developed to overcome the deficiency of common nano-TiO_2 photocatalysts. The multi-type carbon species were derived from tetrabutyl titanate and ethanol as the internal and external carbon sources, respectively. Meanwhile, diverse characterization methods were applied to investigate the morphology and surface properties of the photocatalyst. Finally, the visible-light photocatalytic degradation activity of the collected samples was evaluated by using methyl orange as a model pollutant. The promotion mechanism of multi-type carbon species in the photocatalytic process was also discussed and reported. The results in this work show that the doping and modification of multi-type carbon species successfully narrows the bandgap of nano-TiO_2 to expand the light absorption range, reduces the valence band position to improve the oxidation ability of photogenerated holes, and promotes the separation of photogenerated charge carriers to improve quantum efficiency. In addition, the further modification of the external carbon source can promote the surface adsorption of MO and stabilize the multi-type carbon species on the surface of nano-TiO_2.

1 Introduction

In the past several decades of photocatalysis research, nano-TiO_2 as a photocatalyst has been extensively studied due to its low price, non-toxicity, natural abundance, high thermal and chemical stability, and its wide practical application in industry.[1–6] However, the bandgap of nano-TiO_2 is relatively wide ($\geq$3.0 eV), which severely limits its application in the field of visible-light photocatalysis.[7] In addition, nano-TiO_2 displays a low quantum efficiency due to the rapid recombination of photogenerated electrons and holes. In order to expand the light absorption range of nano-TiO_2 to the visible-light region and suppress the recombination of photogenerated carriers to improve the quantum efficiency, numerous efforts have been devoted to the modification of nano-TiO_2.[8,9] Among these studies, as an important modification method, carbon modification and carbon doping has received considerable attention in recent years.

Compared with the doping and modification of other elements, it can be found that the carbon doping and carbon modification of nano-TiO_2 have some particular advantages. Firstly, carbon sources are naturally abundant and diverse. Either external carbon sources such as glucose, acetone, *etc.*, or internal carbon sources such as carbon components contained in titanium sources (such as tetrabutyl titanate, *etc.*) can be used as carbon sources for carbon doping and modification process.[8,10–12] Secondly, carbon exists in various forms, which involve carbon atoms, oxygen-containing carbon species, amorphous carbon, and graphitic carbon, *etc.*[10–14] Furthermore, the sites of carbon doping and modification are diverse, including the interstitial structure of TiO_2, the substitution of lattice oxygen or titanium sites, the surface of TiO_2, and the interface of nano-TiO_2 particles. Finally, the carbon species possess multiple functions, containing reducing the bandgap, promoting the separation of photogenerated charge carriers, and inducing the visible-light activity of TiO_2 through photosensitization.[15] Therefore, the carbon doping and carbon modification of nano-TiO_2 have been widely investigated in recent years with different synthesis strategies and diversified perspectives.[13,16–20] Nevertheless, due to the diversity of the carbon species,[21–23] an in-depth understanding of the structure of carbon species and the synergistic promotion of the photocatalytic activity of nano-TiO_2 by multi-type carbon species is still deficient.

---

[a] *Inner Mongolia Key Laboratory of Theoretical and Computational Chemistry Simulation, Inner Mongolia University of Technology, Hohhot 010051, China. E-mail: liujuming@imut.edu.cn; jzhang@imut.edu.cn*

[b] *School of Chemical Engineering, Inner Mongolia University of Technology, Hohhot 010051, China*

[c] *School of Energy and Power Engineering, Inner Mongolia University of Technology, Hohhot 010051, China*

† Electronic supplementary information (ESI) available. See DOI: 10.1039/d0ra08894c

In this work, multi-type carbon doped and modified anatase nano-TiO_2 particles were synthesized *via* hydrothermal and low-temperature (300 °C) carbonization process. The carbon component contained in the titanium source tetrabutyl titanate acts as an internal carbon source to form *in situ* carbon doping in the nano-TiO_2. Subsequently, the carbon species derived from the external carbon source ethanol modified the surface of nano-TiO_2. The crystal phase, morphology, carbon species structure, energy band structure and photogenerated charge carrier recombination of the photocatalysts have been investigated by various characterization techniques. Using methyl orange (MO) as a model pollutant, the visible-light photocatalytic degradation activity of the samples was evaluated and the dominant active species were analyzed. Finally, the promotion of different types of carbon species on the photocatalytic activity of nano-TiO_2 was analyzed and discussed.

2 Experiments

2.1 Preparation of photocatalysts

The main reagents used in the preparation of the photocatalysts include: tetrabutyl titanate ($Ti(BuO)_4$) (Aladdin, analytically pure, ≥99%), absolute ethanol (Tianjin Yongsheng Fine Chemical Co., Ltd., analytically pure), distilled water (laboratory self-made).

The photocatalyst preparation process was as below: tetrabutyl titanate (30 mL) and distilled water (6.5 mL) were mixed and reacted in a 100 mL Teflon-lined stainless-steel autoclave (Anhui Kemi Machinery Technology Co., Ltd.) with continuously stirring at the room temperature for 1 h. Afterwards, the autoclave was placed in an oven and kept at 180 °C for 12 h for hydrothermal reaction. After the reaction, the collected solid product was washed three times with distilled water and ethanol to remove impurities, and then dried at 80 °C for 2 h. The obtained sample was labeled as AT. Then, the obtained AT sample in a crucible was placed in a muffle furnace. After carbonizing in air at 300 °C for 2 h, the resulting sample was labeled as C_dAT. After that, the C_dAT sample (0.3 g) was mixed with absolute ethanol (9 mL) in a crucible, and then placed in a tube furnace and carbonized again at 300 °C in an air atmosphere for 2 h. The resulting sample was labeled as C_mC_dAT, in which AT means anatase nano-TiO_2, C_d means doped with carbon species, C_m means modified by carbon species.

Fig. S1† shows the photographs of the as-prepared samples. Compared with the white AT sample, the sample C_dAT is light yellow, indicating that carbon doping changed the light absorption characteristics of nano-TiO_2. Compared with the C_dAT sample, the C_mC_dAT sample was dark brown, indicating that the carbon modification caused a further change in the light absorption characteristics of the nano-TiO_2.

2.2 Characterization of photocatalysts

The crystal structure of the samples was analyzed by a Smartlab 9 kW X-ray diffractometer from Rigaku (Japan) using Cu Kα radiation. The test voltage was 200 kV, the test current was 45 mA, and the scanning speed was 2° min^{-1}. The morphology of the samples was observed by transmission electron microscopy (TEM, FEI Talos 200X) and scanning electron microscopy (SEM, Hitachi-SU 8220). A NETZSCH STA 449 F5/F3 Jupiter thermal analysis system (Germany) was used for the thermal gravimetric (TG) characterization of the as-prepared samples. The measuring temperature range was 30–1100 °C, the heating rate was 10.0 °C min^{-1}, and the measuring atmosphere was air. N_2 adsorption–desorption isotherms were collected by a Micromeritics ASAP 2020 volumetric adsorption analyzer (USA) at 77 K. Prior to the measurement, the samples were degassed at 200 °C for 10 h. The Brunauer–Emmett–Teller (BET) method was utilized to calculate the specific surface area. Pore size distribution was derived from the desorption branch using Barrett–Joyner–Halenda (BJH) method. The total pore volume was estimated from the adsorbed amounts at a relative pressure (P/P_0) of 0.99. A Thermo-Fisher ESCAlab 250Xi X-ray photoelectron spectrometer with Al Kα X-ray source was used to analyze the X-ray photoelectron spectroscopy (XPS) of the samples. Attenuated total reflection Fourier transform infrared spectroscopy (ATR-FTIR) was performed using a PerkinElmer Frontier Fourier transform infrared spectrometer equipped with an attenuated total reflection accessory. An ultraviolet-visible spectrometer (UV-3600, Shimadzu, Japan) was used with barium sulfate ($BaSO_4$) as a reference and the ultraviolet-visible diffuse reflectance spectrum (UV-Vis DRS) was recorded in the range of 200–800 nm in order to analyze the light response range of the samples. The photoluminescence spectra of the samples were recorded at an excitation wavelength of 450 nm by using a FLS 980 spectrometer (Edinburgh Instruments) to characterize the recombination of photogenerated charge carriers.

2.3 Evaluation of visible-light photocatalytic activity

MO was used as a model pollutant in water to evaluate the visible-light photocatalytic degradation activity of the as-prepared samples. The light source is a 20 W blue LED lamp with a wavelength of 450 nm, and its emission spectrum is shown in Fig. S2.† The specific experimental procedure is as follows: photocatalyst (0.1 g) was placed in a 50 mL quartz reactor, and then MO solution (20 mg L^{-1}, 30 mL) was added with stirring for 60 min until MO reached adsorption–desorption equilibrium on the photocatalyst, then turned on the light source and irradiated for 180 min with continuous stirring to carry out the photocatalytic reaction. About 3 mL of suspension was drawn from the reactor every 30 min and passed through a Millipore filter (pore size 0.22 μm) to remove solid particles. Then, the absorbance of the solution was analyzed by a UV-Vis spectrometer, and the degradation rate of MO on the photocatalyst was calculated based on the linear relationship between the absorbance at 464 nm (the characteristic absorption wavelength of MO) and the concentration of the MO solution. The liquid was poured back into the reactor after analyzed.

The cyclic degradation performance of the photocatalyst was evaluated using an "*in situ*" cyclic degradation mode without separating the photocatalyst. The specific steps were as follows: the photocatalyst was not separated after the first round of photocatalytic degradation. Keeping the total volume of the degradation suspension system unchanged, MO was directly added to the system until the absorbance reached the initial value of the first round of degradation. Then, the second round of photocatalytic degradation was carried out under the same conditions as the first round of degradation. The subsequent cycle of degradation repeated the second round of degradation until the fifth round of degradation was completed.

2.4 Analysis of dominant active species in the photocatalytic process

To study the photocatalytic reaction mechanism, it is necessary to analyze the effect and influence of the active species which play a major role in the degradation process of MO. The photocatalytic degradation reaction mechanism can be divided into three typical reaction processes: firstly, photogenerated holes are as the leading factor; secondly, hydroxyl radicals are as the leading factor; thirdly, superoxide radicals are as the leading factor. Therefore, the corresponding sacrificial reagents including triethanolamine (TEOA, scavengers for holes, Tianjin Yongsheng Fine Chemical Co., Ltd., analytical grade),[20] methanol (MeOH, scavengers for hydroxyl radicals, Tianjin Yongsheng Fine Chemical Co., Ltd., analytical grade)[20,24] and *p*-benzoquinone (PBQ, scavengers for superoxide radicals, Aladdin, China Reagent Co., Ltd., analytically pure)[25] were selected for active species inhibition experiments. In the experiment, different concentrations of sacrificial reagents (3.79 mM TEOA, 8 mM MeOH, 0.18 mM PBQ) solutions were added to the photocatalytic degradation system.[20] The other experimental steps were the same as the aforementioned photocatalytic degradation of MO. The dominant active species were judged based on the change in photocatalytic degradation activity.

3 Results and discussions

3.1 Morphology and structure analysis

Fig. 1 shows the XRD spectra of the prepared AT, C_dAT and C_mC_dAT samples. Compared with the standard spectrum of TiO_2, it is evident that the characteristic peaks of the three samples belong to the anatase phase (JCPDS no. 99-0008), and no characteristic diffraction peaks of other crystal phases such as rutile and brookite are observed. Compared with the AT sample, the (101) peak intensity of the C_dAT and C_mC_dAT samples is slightly lower, which is related to the X-ray interface scattering caused by some surface species on the TiO_2.[25,26] Combined with the sample preparation process, these surface species were carbonized products derived from the carbon-containing titanium source (internal carbon source) and ethanol (external carbon source).

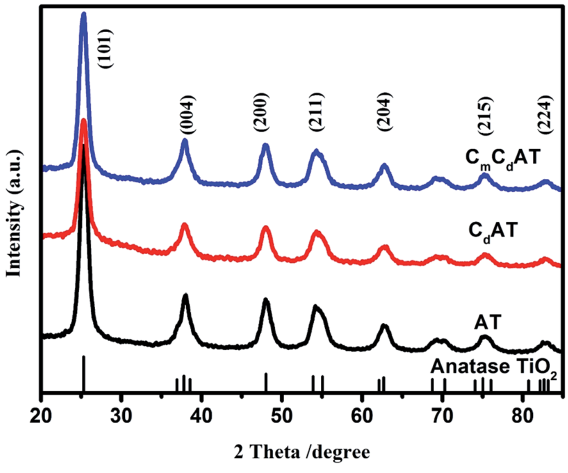

Fig. 1 XRD patterns of the as-prepared samples.

The morphology of the prepared samples was observed by using SEM and TEM techniques. Fig. S3† shows the SEM images of the three samples and the corresponding EDS elemental mapping images. As shown in Fig. S3(a1, a2, b1, b2, c1 and c2),† the three samples have the same morphological characteristics, and they are all formed by random agglomeration of nanoparticles. This observation indicates that the doping and modification of carbon species does not significantly alter the morphology of nano-TiO_2. It can be seen from the corresponding EDS mapping results (Fig. S3(a3–a6, b3–b6 and c3–c6)†) that the distribution of elements is relatively uniform, and no local enrichment of elements is observed. In particular, the distribution of carbon elements is very even, indicating that the doping and modification of nano-TiO_2 by the carbon species introduced by the internal and external carbon sources is uniform.

Fig. 2 and S4† show the TEM characterization results of the samples. It can be observed that the particle size of nano-TiO_2 is around 10 nm, and these TiO_2 nano-particles randomly and irregularly agglomerate into dozens of nano-sized secondary particles, which is consistent with the SEM results. The HRTEM observation of the three samples (Fig. 2) further confirms that the spacing of the lattice fringes is around 0.35 nm, which is consistent with the spacing of the (101) facets of tetragonal anatase, as revealed by the XRD results. Compared with the original AT sample (Fig. 2(a)), the C_dAT sample (Fig. 2(b)) has no obvious difference in morphology, indicating that low-temperature carbonization has no effect on the morphology and crystal phase of nano-TiO_2. It is worth noting that for the C_mC_dAT sample with the highest carbon content, a very thin surface carbon layer can be observed (as shown in Fig. 2(c)), which indicates that the carbon species derived from the external carbon source ethanol was successfully modified on the surface of the nano-TiO_2.

In order to determine the carbon species loading of each sample, TG analysis was performed, and the results are shown in Fig. S5.† The carbon species loadings of the samples estimated from the TG results were summarized in Table 1. Compared with the AT and C_dAT samples, the carbon species loading of the C_mC_dAT sample increases by about 10 times. Notably, the C_mC_dAT sample has one more stage of weight loss than the AT and C_dAT samples (Fig. S5†), indicating that the modification of ethanol has introduced more types of carbon species. In addition, the AT and C_dAT samples ended their weight loss at about 700 °C, while the weight loss of the C_mC_dAT sample extended to more than 1000 °C, indicating that the carbon species of the C_mC_dAT sample has better stability.

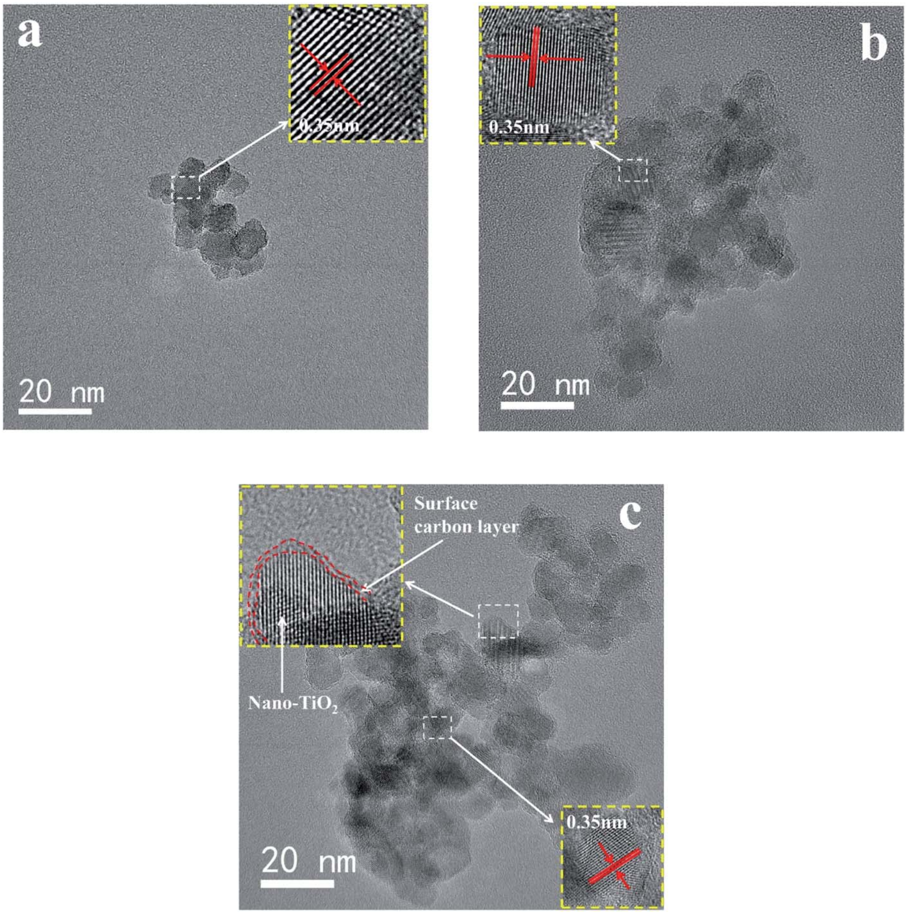

Fig. 2 TEM and HRTEM (illustrations) images of the (a) AT, (b) C_dAT and (c) C_mC_dAT samples.

N_2 adsorption–desorption isotherm measurements were also performed to investigate the specific surface area and pore size distribution of the samples. The BET specific surface area and BJH average pore diameter calculated from the N_2 adsorption–desorption data were summarized in Table 1. The N_2 adsorption–desorption isotherms of all the samples (Fig. S6(a1, b1 and c1)†) show a typical type-IV behavior with a H_2-type hysteresis loop, indicating the existence of uniform mesopores.[27] The pore size distribution plots (Fig. S6(a2, b2 and c2)†) and the average pore diameter data in Table 1 further confirm this result. The AT sample that has not been heat-treated exhibits the highest BET surface area and the smallest pore size. Compared with the AT sample, the BET surface area of the C_dAT sample is reduced and the pore diameter is increased. In addition, as shown in Fig. S6(b2),† the C_dAT sample has a new mesopore distribution at the pore diameter of 9.04 nm. These results indicate that the volatilization and carbonization of carbon species during the carbonization process lead to the destruction of some pores, resulting in an increase in pore size and a decrease in BET surface area. After the C_dAT sample was modified with ethanol, the resulting C_mC_dAT sample exhibited the lowest BET surface area and lower average pore size. At the same time, the mesopore distribution of 9.04 nm disappeared, as shown in Fig. S6(c2).† These results should be attributed to the surface deposition of a large amount of carbon species derived from the external carbon source ethanol, which resulted in the blockage of some pores and the reduction of BET surface area and pore size. All three samples have uniformly distributed mesopores around 7.2 nm. It is generally agreed that the mesoporous TiO_2 materials possess better photocatalytic performance due to their larger surface area, more accessible active sites, facilitated diffusion of reactants and multiple scattering of incident light.[28–33]

Table 1 The carbon species loading, BET surface area and average pore diameter of the AT, CdAT and C_mC_dAT samples

Sample	Carbon species loading (%)	BET surface area (m^2 g^{-1})	Average pore diameter (nm)
AT	1.00	187.78	7.78
C_dAT	1.35	174.99	8.47
C_mC_dAT	14.02	120.46	8.36

3.2 Surface chemical analysis

To investigate the surface chemistry of the samples, ATR-FTIR characterization and analysis were conducted on three samples. As shown in Fig. 3, the attribution analysis of the infrared characteristic absorption bands is as below. The broad absorption bands locate near 3280 cm^{-1} and 3210 cm^{-1} are the characteristics of absorption from the stretching vibrations of the hydroxyl groups in the hydrogen-bond network on the TiO_2 surface.[34–36] The absorption band at 1640 cm^{-1} corresponds to the bending vibration of the adsorbed water molecules on the TiO_2 surface in the hydrogen bond network.[36–38] The characteristic absorption bands at 2960 cm^{-1} and 2868 cm^{-1} are attributed to the antisymmetric and symmetric stretching vibrations of methyl groups,[39] and the characteristic absorption bands at 2920 cm^{-1} are attributed to the antisymmetric stretching vibration of methylene,[40] and the methylene stretching vibration with weaker peak intensity appears at 1380 cm^{-1}.[41,42] The characteristic absorption bands at 1090 cm^{-1} and 1050 cm^{-1} are attributed to the stretching vibration absorption of the ethanol C–OH bond.[43–45] In addition, the characteristic absorption band at 1700 cm^{-1} should be attributed to the carbonyl stretching vibration of the carboxylic acid dimer.[46–50] The characteristic absorption bands at 1582 cm^{-1} and 1440 cm^{-1} are attributed to the antisymmetric and symmetric stretching vibration of the coordinated carboxyl group on the surface of TiO_2.[43,44,51] The appearance of carboxylic acid is resulted from the oxidation of alcohol in the hydrothermal process and carbonization process. Similar results have been observed in our previous studies.[16] ATR-FTIR spectroscopy is also a reliable method to determine the coordination mode of carboxyl groups. The frequency difference between the antisymmetric and symmetric stretching vibrations of the carboxyl group ($\Delta = \nu_{as} - \nu_s$) is directly related to its coordination mode. Generally, the frequency difference for monodentate binding is 350–500 cm^{-1} and for bidentate chelating it is 60–100 cm^{-1}, while the frequency difference for bidentate bridging is between the former two.[52,53] As shown in Fig. 3, the Δ values of the C_dAT and C_mC_dAT samples are both 88 cm^{-1}, indicating that the coordination mode of the carboxyl group is bidentate chelating.

For the AT sample, there are a large number of hydroxyl groups and adsorbed water molecules on the surface to form a hydrogen-bond network. The hydrogen-bond also caused the AT sample to adsorb a certain amount of ethanol molecules when it was washed by ethanol, resulting in the appearance of the infrared characteristic absorption of ethanol. In the hydrothermal process, the butanol produced from the hydrolysis of tetrabutyl titanate was also adsorbed on the surface of the AT sample, which leaded to the infrared characteristic absorption of methyl and methylene groups of the AT sample. After the AT sample was carbonized at 300 °C, the amount of hydroxyl groups and adsorbed water on the surface of the obtained C_dAT sample was greatly reduced, and the infrared absorption characteristic bands of ethanol and butanol almost disappeared, and the characteristic band intensity of the carboxyl coordination structure at 1582 cm^{-1} and 1440 cm^{-1} increased. These results indicate that a large amount of hydroxyl and water adsorbed on the surface of TiO_2 volatilized in the carbonization process, part of the ethanol and butanol adsorbed on the surface also volatilized, and the rest of them were carbonized, oxidized, and converted into carbon species with carboxyl groups. For the C_mC_dAT sample, the surface hydroxyl content further decreased, and the surface adsorbed water molecules almost disappeared. Meanwhile, the obvious infrared absorption characteristics of ethanol were observed, the infrared absorption of methyl and methylene groups was significantly enhanced, and the content of bidentate chelated carboxylate ligands obviously increased, and even the infrared absorption characteristics of carboxylic acid dimer occurred at 1700 cm^{-1}. These results show that the external carbon source ethanol was oxidized on the surface of nano-TiO_2 in the carbonization process, and carbonized to generate a series of carbon species, including alcohols, bidentate carboxylate ligands and carboxylic acid dimers. These carbonized carbon species replaced the surface hydroxyl groups and the adsorbed water molecules, and eventually succeeded as the dominant surface species on nano-TiO_2.

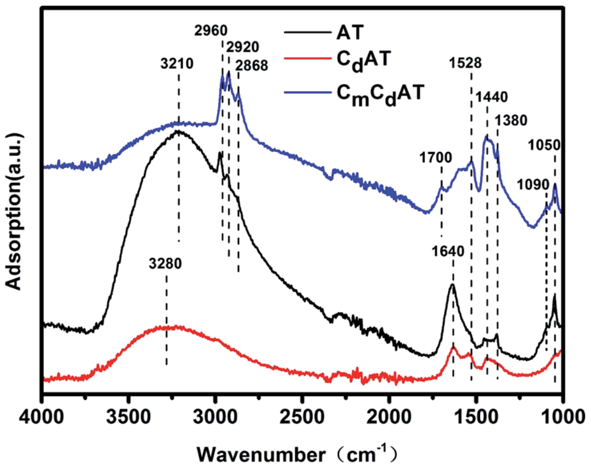

Fig. 3 ATR-FTIR spectra of the as-prepared samples.

In order to further investigate the surface chemical state of the samples, XPS characterization was performed and the results were shown in Fig. 4. All XPS data was corrected according to the C 1s peak of the C–C bond at 284.8 eV. As shown in Fig. 4(a), the surfaces of the three samples only contain the elements Ti, O, and C, and no other elements are observed. Fig. 4(b) shows the C 1s high-resolution XPS spectra of the samples. The C 1s peaks at 284.8 eV, 285.8–286.2 eV and 288.8–289.1 eV correspond to the C–C, C–O and COO bonds, respectively.[54,55] Notably, on the one hand, these C 1s peaks further confirm the existence of multi-type carbon species, which is revealed by the results of ATR-FTIR. On the other hand, the latter two C 1s peaks (C–O and COO bonds) also demonstrate the presence of carbonate doping in nano-TiO_2.[13] Meanwhile, the C 1s characteristic peak of the C–Ti bond was not observed at 282.0 eV,[10] indicating that the lattice oxygen was not substituted by carbon. Fig. 4(c) shows the Ti 2p high-resolution XPS spectra of the samples. The characteristic peaks at 458.6–458.9 eV correspond to the Ti $2p_{3/2}$ binding energy region, and the characteristic peaks at 464.3–464.6 eV correspond to the Ti $2p_{1/2}$ binding energy region.[54,55] Following the order of AT, C_dAT and C_mC_dAT, the position of the characteristic peak of Ti 2p gradually shifts toward the direction of higher binding energy. Considering that XPS is a surface detection technology, this change should be related to the succession of the surface

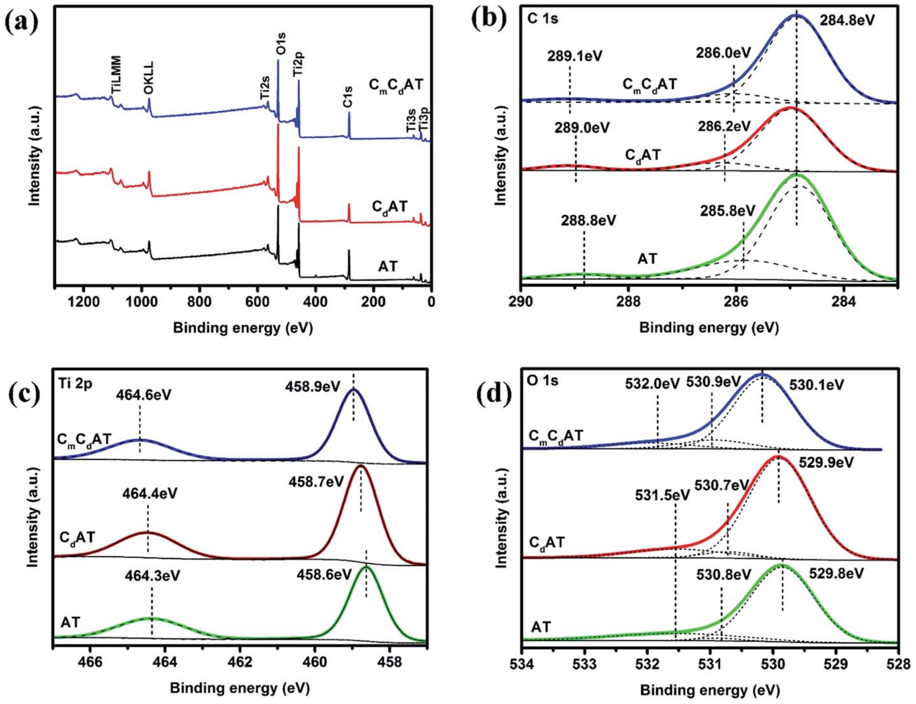

Fig. 4 (a) XPS survey spectra and high-resolution (b) C 1s, (c) Ti 2p and (d) O 1s XPS spectra of the as-prepared samples.

species of nano-TiO_2. According to the ATR-FTIR results, following the order of AT, C_dAT and C_mC_dAT, the dominant surface species of nano-TiO_2 succeeded from hydroxyl and adsorbed water molecules to multi-type carbon species involving carboxyl and carbonyl. The electron-withdrawing carboxyl and carbonyl groups reduce the local electron density of Ti cations, leading to an increase in the binding energy of Ti 2p. A similar trend can also be observed in the O 1s high-resolution spectra of the samples, as shown in Fig. 4(d). The peaks at 529.8–530.1 eV, 530.7–530.9 eV and 531.5–532.0 eV correspond to lattice oxygen, surface hydroxyl and water molecules, surface carboxyl groups and other oxygen-containing carbon species, respectively.[54]

3.3 Energy band structure analysis

The bandgap and valence band (VB) position of the samples were investigated by UV-Vis DRS and VB-XPS. Based on these data, schematic diagrams of the energy band structure of the samples were drawn.[17,56] The results are shown in Fig. 5. As shown in Fig. 5(a1), the bandgap of the AT sample is 3.20 eV, which is completely consistent with the bandgap of anatase TiO_2. Compared with the AT sample, the light absorption of the C_dAT and C_mC_dAT samples both exhibit a red shift, as shown in Fig. 5(a2 and a3). The bandgaps of the C_dAT and C_mC_dAT samples are 3.16 eV and 2.92 eV, respectively. The results indicate that carbonate doping and multi-type carbon modification can effectively narrow the bandgap of nano-TiO_2. In addition, all three samples exhibit "tail-like" absorption characteristics in the visible-light region. The "tail-like" absorption of the AT sample extends to about 550 nm, while the "tail-like" absorption of the C_dAT and C_mC_dAT samples extends to about 800 nm. The "tail-like" absorption greatly expands the light response range of the samples. These "tail-like" absorptions are mainly attributed to two contributions: one is carbonate doping, and the other is modification of multi-type carbon species. The previous results have shown that carbonate doping can introduce diffused VB tail states at the VB edge, which can narrow the bandgap of TiO_2.[13] The VB-XPS spectra of the three samples shown in Fig. 5(b1–b3) confirm the presence of the VB tail states. In addition, the carbonized multi-type carbon species on the surface of the C_dAT and C_mC_dAT samples can also work as photosensitizers to induce the visible-light photocatalytic activity of nano-TiO_2, as demonstrated by the previous results.[57,58]

As shown in Fig. 5(b1–b3), the VB edges of the AT, C_dAT, and C_mC_dAT samples are located at 2.68, 2.74, and 2.88 eV, respectively, showing a gradually increasing trend. This result is consistent with the increasing trend of the binding energy of Ti 2p and O 1s peaks, which should also be attributed to the electron-withdrawing carboxyl and carbonyl groups. Based on the results of UV-Vis DRS and VB-XPS spectra, the energy band structures of the AT, C_dAT, and C_mC_dAT samples are schematically drawn in Fig. 5(c1–c3). According to the VB-XPS spectra, the VB edges of the AT, C_dAT, and C_mC_dAT samples are located at 2.68, 2.74, and 2.88 eV, respectively. The UV-Vis DRS spectra demonstrate that the bandgaps of the three samples are 3.20 eV, 3.16 eV, and 2.92 eV, respectively. Therefore, their corresponding conduction band minimum (CBM) would occur at −0.52 eV, −0.42 eV, and −0.04 eV, respectively. Because of the existence of the VB tail states, the valence band maximum (VBM) energies are located at 2.12, 2.22, and 2.47 eV, respectively. Finally, the

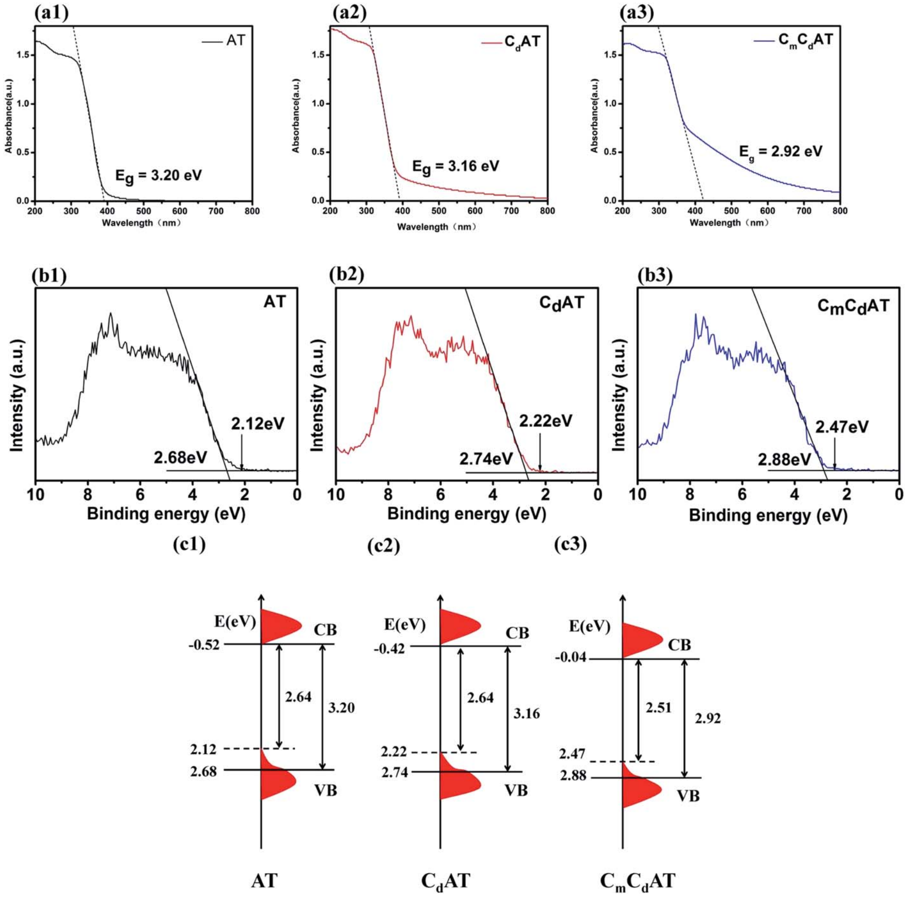

Fig. 5 UV-vis DRS spectra ((a1)–(a3)), VB-XPS spectra ((b1)–(b3)) and proposed schematic energy band structures ((c1)–(c3)) of the as-prepared samples.

bandgaps of the AT, C_dAT and C_mC_dAT samples are 2.64 eV, 2.64 eV and 2.51 eV, respectively. That is, based on the red shift of the light absorption edge, the VB tail states further narrow the bandgaps of the samples, which enables the multi-type carbon doped and modified nano-TiO_2 to harvest more visible-light. In addition, it is worth noting that following the sequence of AT, C_dAT and C_mC_dAT, the position of the VB edge gradually shifts downward, which is beneficial to enhance the oxidative degradation ability of the photogenerated holes of the photocatalysts.

3.4 Analysis of the recombination of photogenerated charge carriers

To investigate the recombination of photogenerated charge carriers, the prepared samples were characterized by PL emission spectra. PL emission spectra have been frequently used to investigate the efficiency of charge carrier trapping, migration, and transfer in order to understand the fate of electron–hole pairs in semiconductor particles because PL emission results from the recombination of free carriers.[15] As shown in Fig. 6, PL spectra are examined at the excitation wavelengths of 450 nm and show peaks at different wavelengths that indicate the trap sites present on the surface of the photocatalyst. The PL spectra show the change in the peak intensity of the three as-prepared samples, increasing in the following sequence: $C_mC_dAT < C_dAT < AT$. This result indicates that the multi-type carbon species derived from internal and external carbon sources are efficient to inhibit the recombination of photogenerated charge carriers.

3.5 Analysis of photocatalytic activity and dominant active species

The visible-light photocatalytic activity of the samples was evaluated using MO as a model pollutant, and the results are shown in Fig. 7(a). In a dark environment, the sample can reach the adsorption–desorption equilibrium of MO within 60 min. At this stage, the AT sample has no obvious adsorption of MO. The C_dAT sample modified by the internal carbon source adsorbed about 15% of MO, while the C_mC_dAT sample modified by the external carbon source adsorbed about 20% of MO. This result indicates that the multi-type carbon species promotes the surface adsorption of MO, which is conducive to further photocatalytic degradation of MO. In the subsequent photocatalytic process, the AT sample showed weaker photocatalytic activity, while the C_dAT and C_mC_dAT samples both showed higher photocatalytic activity, and the final degradation rate after 120 min was close to 100%. Based on the aforementioned

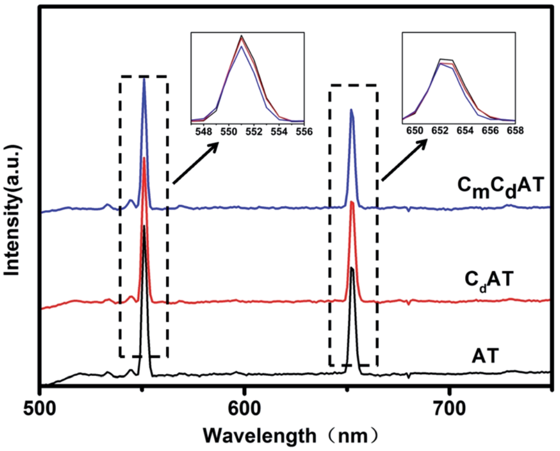

Fig. 6 Photoluminescence spectra of the as-prepared samples with the excitation wavelength at 450 nm.

characterizations and analyses, the excellent photocatalytic activity of the C_dAT and C_mC_dAT samples are due to: (1) the doping and modification of multi-type carbon species leads to the narrowing of the bandgap of nano-TiO_2 and the red shift of the light absorption edge; (2) the multi-type carbon species further narrows the bandgap of nano-TiO_2 by introducing the VB tail state; (3) the electron-withdrawing carboxyl and carbonyl groups of multi-type carbon species induce nano-TiO_2 to form lower VB positions, which significantly enhances the oxidative degradation ability of photogenerated holes; (4) multi-type carbon species promote the separation of photo-generated charge carriers; (5) multi-type carbon species significantly increase the surface adsorption of MO, which is beneficial to the rapid photocatalytic degradation of MO.

Fig. 7(b) and (c) are the results of the cyclic photocatalytic degradation of the C_mC_dAT and C_dAT samples. In a dark environment, the C_mC_dAT sample exhibited higher adsorption of MO than the C_dAT sample, which proved that the multi-type carbon species can effectively promote the surface adsorption of MO. After five rounds of *in situ* photocatalytic degradation, the degradation rate of C_mC_dAT samples can still reach 90%, while the degradation rate of C_dAT samples drops to 46%. The stable photocatalytic performance of the C_mC_dAT sample should be attributed to the dominant multi-type carbon species on its surface. According to the ATR-FTIR results, the surface of the C_mC_dAT sample has almost no adsorbed water molecules. Therefore, the C_mC_dAT sample has a relatively hydrophobic surface. On the contrary, the surface of the C_dAT sample has a certain amount of adsorbed water molecules, indicating that it has a certain hydrophilicity. The dissociative adsorption of water molecules may destroy the structure of the surface carbon species of nano-TiO_2.[36] In addition, the TG results also show that the carbon species of the C_mC_dAT sample has better stability. Therefore, the stable hydrophobic surface can protect the surface multi-type carbon species of the C_mC_dAT sample and make the sample exhibit stable cyclic photocatalytic degradation performance.

In order to clarify the dominant active species in the photocatalytic process, the free radical suppression experiment and

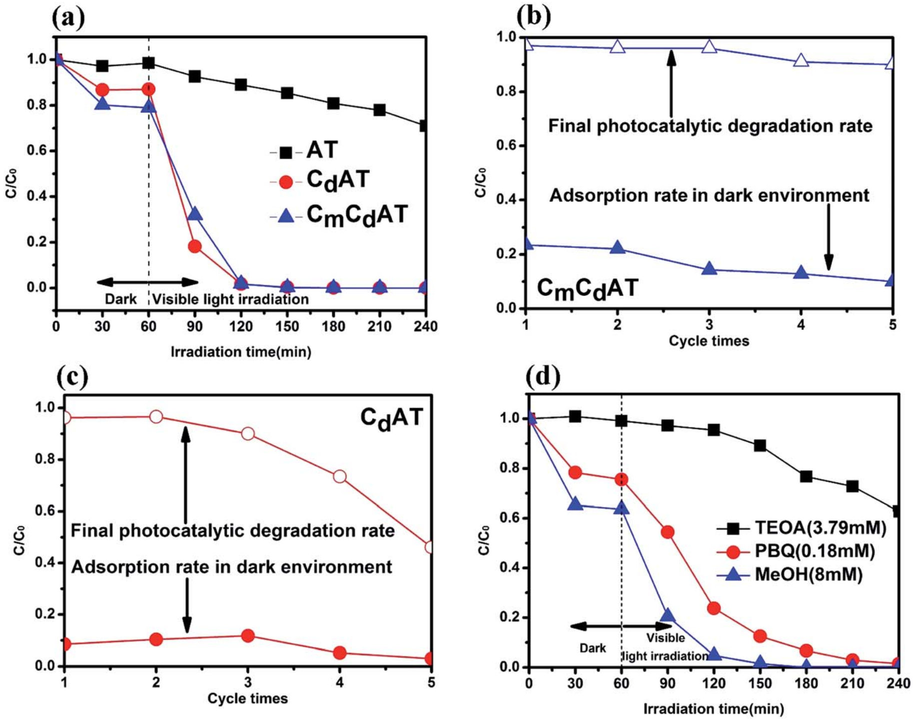

Fig. 7 (a) Photocatalytic degradation of MO by the as-prepared samples under blue LED (450 nm) irradiation. In the *in situ* cyclic degradation process of the (b) C_mC_dAT and (c) C_dAT samples, the adsorption rate of MO in the dark environment and the photocatalytic degradation rate under blue LED irradiation in each round. (d) Photocatalytic degradation of MO by the C_mC_dAT sample with different scavengers.

analysis were carried out with the C_mC_dAT sample as a representative sample. TEOA, MeOH, and PBQ were used as sacrificial reagents for photogenerated holes (h^+), hydroxyl radicals ($^{\bullet}OH$) and superoxide radicals ($^{\bullet}O_2^-$) to identify the dominant active species. The results are shown in Fig. 7(d). The addition of MeOH to the reaction system did not result in a significant decrease in the photocatalytic activity, which means that $^{\bullet}OH$ is not the dominant active species. When PBQ was added to the reaction system, the photocatalytic activity decreased, indicating that $^{\bullet}O_2^-$ is an active species that played a role in the photocatalytic process. It is worth noting that the addition of TEOA to the system led to a significant decrease in the photocatalytic activity, which indicates that photogenerated h^+ is the active species that played a major role in the photocatalytic process.

4 Conclusion

Multi-type carbon species doped and modified anatase nano-TiO_2 photocatalysts were synthesized *via* hydrothermal and low-temperature (300 °C) carbonization processes by using the carbon components contained in tetrabutyl titanate and ethanol as the internal and the external carbon sources, respectively. Multi-type carbon species involve carbonates, adsorbed alcohols, bidentate carboxylate ligands, and adsorbed carboxylic acid dimers. The doping and modification of multi-type carbon species can narrow the bandgap of nano-TiO_2 to expand the light absorption range, shift the VB position down to improve the oxidation ability of photogenerated holes, and promote the separation of photogenerated charge carriers to improve quantum efficiency. In addition, the stable hydrophobic surface caused by the modification of multi-type carbon species promotes the adsorption of MO and stabilizes the multi-type carbon species on the surface of nano-TiO_2. The synergy of the above factors resulted in the C_mC_dAT sample exhibiting prominent visible-light photocatalytic degradation activity. The conclusions of this work provide a comprehensive understanding of carbon doping and carbon modification of nano-TiO_2, and develop a convenient and low-cost strategy for the modification of nano-TiO_2.

Author contributions

Conceptualization, methodology, investigation, analysis, and writing, Jianing Li and Juming Liu; writing—original draft preparation, Jianing Li; writing—review and editing, Juming Liu, Junzhong Wang, Yan Li and Huiyan Ma; project administration, Qiancheng Zhang; funding acquisition, Juming Liu and Jucai Yang. All authors have read and agreed to the published version of the manuscript.

Funding

This research was funded by the National Natural Science Foundation of China, Grant No. 21763020; the Natural Science Foundation of the Inner Mongolia Autonomous Region, Grant No. 2018MS02018; the Science Research Project of Inner Mongolia University of Technology, Grant No. x201505 and the Program for Innovative Research Team in Universities of Inner Mongolia Autonomous Region, Grant No. NMGIRT-A1603.

Conflicts of interest

The authors declare no conflict of interest.

Acknowledgements

The authors thank the technical support from the Test Center of Inner Mongolia University of Technology.

References

1 E. J. W. Crossland, N. Noel, V. Sivaram, T. Leijtens, J. A. Alexander-Webber and H. J. Snaith, Mesoporous TiO_2 single crystals delivering enhanced mobility and optoelectronic device performance, *Nature*, 2013, **495**, 215–219.

2 K. Reilly, B. Fang, F. Taghipour and D. P. Wilkinson, Simple and Scalable Synthesis of Vertically Aligned Anatase Nanowires for Enhanced Photoelectrochemical Performance, *ACS Appl. Energy Mater.*, 2020, **3**, 8317–8329.

3 K. Reilly, B. Fang, F. Taghipour and D. P. Wilkinson, Enhanced photocatalytic hydrogen production in a UV-irradiated fluidized bed reactor, *J. Catal.*, 2017, **353**, 63–73.

4 N. P. Chadwick, A. Kafizas, R. Quesada-Cabrera, C. Sotelo-Vazquez, S. M. Bawaked, M. Mokhtar, S. A. Al Thabaiti, A. Y. Obaid, S. N. Basahel and J. R. Durrant, Ultraviolet Radiation Induced Dopant Loss in a TiO_2 Photocatalyst, *ACS Catal.*, 2017, **7**, 1485–1490.

5 K. C. Christoforidis and M. Fernandez-Garcia, Photoactivity and charge trapping sites in copper and vanadium doped anatase TiO_2 nano-materials, *Catal. Sci. Technol.*, 2016, **6**, 1094–1105.

6 A. A. Umar, S. K. Md Saad, M. I. Ali Umar, M. Y. A. Rahman and M. Oyama, Advances in porous and high-energy (001)-faceted anatase TiO_2 nanostructures, *Opt. Mater.*, 2018, **75**, 390–430.

7 V. Etacheri, C. Di Valentin, J. Schneider, D. Bahnemann and S. C. Pillai, Visible-light activation of TiO_2 photocatalysts: advances in theory and experiments, *J. Photochem. Photobiol., C*, 2015, **25**, 1–29.

8 S. U. M. Khan, M. Al-Shahry and W. B. Ingler, Efficient Photochemical Water Splitting by a Chemically Modified n-TiO_2, *Science*, 2002, **297**, 2243–2245.

9 G. Liu, L. Wang, H. G. Yang, H.-M. Cheng and G. Q. Lu, Titania-based photocatalysts-crystal growth, doping and heterostructuring, *J. Mater. Chem.*, 2010, **20**, 831–843.

10 L. Zhang, M. S. Tse, O. K. Tan, Y. X. Wang and M. Han, Facile fabrication and characterization of multi-type carbon-doped TiO_2 for visible light-activated photocatalytic mineralization of gaseous toluene, *J. Mater. Chem. A*, 2013, **1**, 4497–4507.

11 D.-e. Gu, Y. Lu, B.-c. Yang and Y.-d. Hu, Facile preparation of micro-mesoporous carbon-doped TiO_2 photocatalysts with

anatase crystalline walls under template-free condition, *Chem. Commun.*, 2008, 2453–2455.

12 S. Wang, L. Zhao, L. Bai, J. Yan, Q. Jiang and J. Lian, Enhancing photocatalytic activity of disorder-engineered C/TiO_2 and TiO_2 nanoparticles, *J. Mater. Chem. A*, 2014, **2**, 7439–7445.

13 B. Liu, L.-M. Liu, X.-F. Lang, H.-Y. Wang, X. W. Lou and E. S. Aydil, Doping high-surface-area mesoporous TiO_2 microspheres with carbonate for visible light hydrogen production, *Energy Environ. Sci.*, 2014, **7**, 2592–2597.

14 L.-W. Zhang, H.-B. Fu and Y.-F. Zhu, Efficient TiO_2 photocatalysts from surface hybridization of TiO_2 particles with graphite-like carbon, *Adv. Funct. Mater.*, 2008, **18**, 2180–2189.

15 J. Liu, L. Han, N. An, L. Xing, H. Ma, L. Cheng, J. Yang and Q. Zhang, Enhanced visible-light photocatalytic activity of carbonate-doped anatase TiO_2 based on the electron-withdrawing bidentate carboxylate linkage, *Appl. Catal., B*, 2017, **202**, 642–652.

16 Y. Ma, L. Han, H. Ma, J. Wang, J. Liu, L. Cheng, J. Yang and Q. Zhang, Improving the visible-light photocatalytic activity of interstitial carbon-doped TiO_2 with electron-withdrawing bidentate carboxylate ligands, *Catal. Commun.*, 2017, **95**, 1–5.

17 J. Li, Q. Zhang, J. Liu, M. Yu, H. Ma, J. Yang, S. Ye, T. Ramirez Reina and J. Liu, In-situ formation of carboxylate species on TiO_2 nanosheets for enhanced visible-light photocatalytic performance, *J. Colloid Interface Sci.*, 2020, **577**, 512–522.

18 W. Wang, D. Xu, B. Cheng, J. Yu and C. Jiang, Hybrid carbon@TiO_2 hollow spheres with enhanced photocatalytic CO_2 reduction activity, *J. Mater. Chem. A*, 2017, **5**, 5020–5029.

19 R. Djellabi, B. Yang, Y. Wang, X. Cui and X. Zhao, Carbonaceous biomass-titania composites with Ti-O-C bonding bridge for efficient photocatalytic reduction of Cr(VI) under narrow visible light, *Chem. Eng. J.*, 2019, **366**, 172–180.

20 S. Pang, Y. Lu, L. Cheng, J. Liu, H. Ma, J. Yang and Q. Zhang, Facile synthesis of oxygen-deficient nano-TiO_2 coordinated by acetate ligands for enhanced visible-light photocatalytic performance, *Catal. Sci. Technol.*, 2020, **10**, 3875–3889.

21 G. Suo, J. Zhang, D. Li, Q. Yu, W. Wang, M. He, L. Feng, X. Hou, Y. Yang and X. Ye, N-doped carbon/ultrathin 2D metallic cobalt selenide core/sheath flexible framework bridged by chemical bonds for high-performance potassium storage, *Chem. Eng. J.*, 2020, **388**, 124396.

22 D. Li, J. Zhang, S. M. Ahmed, G. Suo, W. Wang, L. Feng, X. Hou, Y. Yang, X. Ye and L. Zhang, Amorphous carbon coated SnO_2 nanosheets on hard carbon hollow spheres to boost potassium storage with high surface capacitive contributions, *J. Colloid Interface Sci.*, 2020, **574**, 174–181.

23 G. Suo, J. Zhang, D. Li, Q. Yu, M. He, L. Feng, X. Hou, Y. Yang, X. Ye and L. Zhang, Flexible N doped carbon/bubble-like MoS_2 core/sheath framework: buffering volume expansion for potassium ion batteries, *J. Colloid Interface Sci.*, 2020, **566**, 427–433.

24 C. Lettmann, K. Hildenbrand, H. Kisch, W. Macyk and W. F. Maier, Visible light photodegradation of 4-chlorophenol with a coke-containing titanium dioxide photocatalyst, *Appl. Catal., B*, 2001, **32**, 215–227.

25 S. Zhao and X. Zhao, Polyoxometalates-derived metal oxides incorporated into graphitic carbon nitride framework for photocatalytic hydrogen peroxide production under visible light, *J. Catal.*, 2018, **366**, 98–106.

26 M. Pelaez, P. Falaras, V. Likodimos, K. O'Shea, A. A. de la Cruz, P. S. M. Dunlop, J. A. Byrne and D. D. Dionysiou, Use of selected scavengers for the determination of NF-TiO_2 reactive oxygen species during the degradation of microcystin-LR under visible light irradiation, *J. Mol. Catal. A: Chem.*, 2016, **425**, 183–189.

27 T. Matthias, K. Katsumi, V. N. Alexander, P. O. James, R.-R. Francisco, R. Jean and S. W. S. Kenneth, Physisorption of gases, with special reference to the evaluation of surface area and pore size distribution (IUPAC Technical Report), *Pure Appl. Chem.*, 2015, **87**, 1051–1069.

28 B. Fang, A. Bonakdarpour, K. Reilly, Y. Xing, F. Taghipour and D. P. Wilkinson, Large-Scale Synthesis of TiO_2 Microspheres with Hierarchical Nanostructure for Highly Efficient Photodriven Reduction of CO_2 to CH_4, *ACS Appl. Mater. Interfaces*, 2014, **6**, 15488–15498.

29 B. Fang, Y. Xing, A. Bonakdarpour, S. Zhang and D. P. Wilkinson, Hierarchical CuO-TiO_2 Hollow Microspheres for Highly Efficient Photodriven Reduction of CO_2 to CH_4, *ACS Sustainable Chem. Eng.*, 2015, **3**, 2381–2388.

30 Y. Xing, S. Wang, B. Fang, G. Song, D. P. Wilkinson and S. Zhang, N-doped hollow urchin-like anatase TiO_2@C composite as a novel anode for Li-ion batteries, *J. Power Sources*, 2018, **385**, 10–17.

31 Y. Xing, B. Fang, A. Bonakdarpour, S. Zhang and D. P. Wilkinson, Facile fabrication of mesoporous carbon nanofibers with unique hierarchical nanoarchitecture for electrochemical hydrogen storage, *Int. J. Hydrogen Energy*, 2014, **39**, 7859–7867.

32 B. Fang, J. H. Kim, M.-S. Kim and J.-S. Yu, Hierarchical Nanostructured Carbons with Meso-Macroporosity: Design, Characterization, and Applications, *Acc. Chem. Res.*, 2013, **46**, 1397–1406.

33 B. Fang, Y. Z. Wei and M. Kumagai, Modified carbon materials for high-rate EDLCs application, *J. Power Sources*, 2006, **155**, 487–491.

34 W.-X. Mao, X.-J. Lin, W. Zhang, Z.-X. Chi, R.-W. Lyu, A.-M. Cao and L.-J. Wan, Core-shell structured TiO_2@polydopamine for highly active visible-light photocatalysis, *Chem. Commun.*, 2016, **52**, 7122–7125.

35 Y. Guo, H. Wang, C. He, L. Qiu and X. Cao, Uniform Carbon-Coated ZnO Nanorods: Microwave-Assisted Preparation, Cytotoxicity, and Photocatalytic Activity, *Langmuir*, 2009, **25**, 4678–4684.

36 Q. Xiang, K. Lv and J. Yu, Pivotal role of fluorine in enhanced photocatalytic activity of anatase TiO_2 nanosheets with dominant (001) facets for the photocatalytic degradation of acetone in air, *Appl. Catal., B*, 2010, **96**, 557–564.

37 V. A. Nadtochenko, A. G. Rincon, S. E. Stanca and J. Kiwi, Dynamics of *E. coli* membrane cell peroxidation during TiO_2 photocatalysis studied by ATR-FTIR spectroscopy and AFM microscopy, *J. Photochem. Photobiol., A*, 2005, **169**, 131–137.

38 H. Zhang, P. Zhou, H. Ji, W. Ma, C. Chen and J. Zhao, Enhancement of photocatalytic decarboxylation on TiO_2 by water-induced change in adsorption-mode, *Appl. Catal., B*, 2018, **224**, 376–382.

39 B. Baumgartner, J. Hayden, J. Loizillon, S. Steinbacher, D. Grosso and B. Lendl, Pore Size-Dependent Structure of Confined Water in Mesoporous Silica Films from Water Adsorption/Desorption Using ATR–FTIR Spectroscopy, *Langmuir*, 2019, **35**, 11986–11994.

40 A. Biancolillo, F. Marini and A. A. D'Archivio, Geographical discrimination of red garlic (*Allium sativum* L.) using fast and non-invasive Attenuated Total Reflectance-Fourier Transformed Infrared (ATR-FTIR) spectroscopy combined with chemometrics, *J. Food Compos. Anal.*, 2020, **86**, 103351.

41 G. Chen, S. Ouyang, Y. Deng, M. Chen, Y. Zhao, W. Zou and Q. Zhao, Improvement of self-cleaning waterborne polyurethane-acrylate with cationic TiO_2/reduced graphene oxide, *RSC Adv.*, 2019, **9**, 18652–18662.

42 C. Rochas, M. Lahaye and W. Yaphe, Sulfate Content of Carrageenan and Agar Determined by Infrared Spectroscopy, *Bot. Mar.*, 1986, **29**, 335–340.

43 R. Viana, A. Silva and A. Pimentel, Infrared Spectroscopy of Anionic, Cationic, and Zwitterionic Surfactants, *Adv. Phys. Chem.*, 2012, **2012**, 1–14.

44 Y. Yu, Z. Hu, C. Li, S. Huang, Z. Chen and H. Gao, Effect of Aging Time on the Characteristics and Photocatalysis of Zn^{2+}-Doped CTAB@BiOCl, *Nano*, 2017, **12**, 1750106–1750115.

45 C. Paluszkiewicz, E. Stodolak, M. Hasik and M. Blazewicz, FT-IR study of montmorillonite-chitosan nanocomposite materials, *Spectrochim. Acta, Part A*, 2011, **79**, 784–788.

46 M. Bensitel, V. Moraver, J. Lamotte, O. Saur and J.-C. Lavalley, Infrared study of alcohols adsorption on zirconium oxide: reactivity of alkoxy species towards CO_2, *Spectrochim. Acta, Part A*, 1987, **43**, 1487–1491.

47 L. Wang, T. Ishiyama and A. Morita, Theoretical Investigation of C-H Vibrational Spectroscopy. 1. Modeling of Methyl and Methylene Groups of Ethanol with Different Conformers, *J. Phys. Chem. A*, 2017, **121**, 6687–6700.

48 X. Du and Y. Liang, Structure Control of Ion Exchange in N-Octadecanoyl-l-alanine Langmuir-Blodgett Films Studied by FTIR Spectroscopy, *Langmuir*, 2000, **16**, 3422–3426.

49 W. Tian, L.-M. Yang, Y.-Z. Xu, S.-F. Weng and J.-G. Wu, Sugar interaction with metal ions. FT-IR study on the structure of crystalline galactaric acid and its K^+, NH^{4+}, Ca^{2+}, Ba^{2+}, and La^{3+} complexes, *Carbohydr. Res.*, 2000, **324**, 45–52.

50 T. Abe, S. Hayashi, N. Higashi, M. Niwa and K. Kurihara, Charge regulation in polyelectrolyte brushes studied by FTIR spectroscopy, *Colloids Surf., A*, 2000, **169**, 351–356.

51 B. Mailhot and J. L. Gardette, Polystyrene photooxidation. 1. Identification of the IR-absorbing photoproducts formed at short and long wavelengths, *Macromolecules*, 1992, **25**, 4119–4126.

52 S. S. Cheng, D. A. Scherson and C. N. Sukenik, *In Situ* Attenuated Total Reflectance Fourier Transform Infrared Spectroscopy Study of Carboxylate-Bearing, Siloxane-Anchored, Self-Assembled Monolayers: A Study of Carboxylate Reactivity and Acid-Base Properties, *Langmuir*, 1995, **11**, 1190–1195.

53 J. Llorca, N. Homs and P. Ramirez de la Piscina, *In situ* DRIFT-mass spectrometry study of the ethanol steam-reforming reaction over carbonyl-derived Co/ZnO catalysts, *J. Catal.*, 2004, **227**, 556–560.

54 D. Zhao, C. Chen, Y. Wang, W. Ma, J. Zhao, T. Rajh and L. Zang, Enhanced Photocatalytic Degradation of Dye Pollutants under Visible Irradiation on Al(III)-Modified TiO_2: Structure, Interaction, and Interfacial Electron Transfer, *Environ. Sci. Technol.*, 2008, **42**, 308–314.

55 Q. Qu, H. Geng, R. Peng, Q. Cui, X. Gu, F. Li and M. Wang, Chemically Binding Carboxylic Acids onto TiO_2 Nanoparticles with Adjustable Coverage by Solvothermal Strategy, *Langmuir*, 2010, **26**, 9539–9546.

56 Y. Zou, J.-W. Shi, D. Ma, Z. Fan, L. Lu and C. Niu, *In situ* synthesis of C-doped TiO_2@g-C_3N_4 core-shell hollow nanospheres with enhanced visible-light photocatalytic activity for H_2 evolution, *Chem. Eng. J.*, 2017, **322**, 435–444.

57 Z. Lu, L. Zeng, W. Song, Z. Qin, D. Zeng and C. Xie, *In situ* synthesis of C-TiO_2/g-C_3N_4 heterojunction nanocomposite as highly visible light active photocatalyst originated from effective interfacial charge transfer, *Appl. Catal., B*, 2017, **202**, 489–499.

58 X. Chen, L. Liu, P. Y. Yu and S. S. Mao, Increasing Solar Absorption for Photocatalysis with Black Hydrogenated Titanium Dioxide Nanocrystals, *Science*, 2011, **331**, 746–750.